Proceedings of the 2nd Biennial IEEE/RAS-EMBS International
Conference on Biomedical Robotics and Biomechatronics
Scottsdale, AZ, USA, October 19-22, 2008

Design of a Rotational Hydro-Elastic Actuator for an Active Upper-Extremity Rehabilitation Exoskeleton.

Arno H.A. Stienen[1,4], Edsko E.G. Hekman[1], Huub ter Braak[2],
Arthur M.M. Aalsma[2], Frans C.T. van der Helm[1,3] and Herman van der Kooij[1,3]

***Abstract*— Our new Limpact exoskeleton is mechanically based on the design of the passive Dampace and will be powered by rotational hydro-elastic actuators (rHEAs), using impedance control. In this paper we describe the design of the rHEA, which is a novel, custom-designed combination of a rotational hydraulic actuator and a symmetric torsion spring. The rHEA can also be used as a springless hydraulic actuator for stiffer admittance control, or for isometric large-torque measurements of up to 100 Nm, by locking specific components in the design.**

Our implementation of HEA required alterations to the existing theoretical models to account for (1) our long flexible tubes between the valve and cylinder, and (2) the influence of the pressure feedback on the valve flow. These newly adapted models gave the best fits on the frequency response functions from our open- and closed-loop identification experiments, and might even provide a better fit for the data in the original publication of the theoretical models.

Multi-sine identification showed the torque-tracking bandwidth restricted to 18 Hz for a constant spectral-density reference signal of 20 Nm, mostly due the transport delays in the long flexible tubes. The measured torque resolution was better then 0.01 Nm. The delivered torque resolution was below 1 Nm, although at those small amplitudes, the output signal was accompanied by significant phase lead indicating some unaccounted for non-linearities in the actuator. When manipulated manually by forefinger and thumb, almost no distortion torques were felt during minimal-impedance and virtual-spring control.

The symmetric torsion spring proved difficult to model correctly, and finding the best design became an iterative process. The spring in the prototype, used for the measurements as reported in this study, had a stiffness and maximum torque below those theoretically calculated, limiting the desired output to 22 Nm. With our latest spring design for the actuators in the Limpact, the maximum output torque is increased to 50 Nm.

I. Introduction

Patient-friendly robotics are used as diagnostic and therapeutic aids in upper-extremities rehabilitation, and almost none look alike. Through physical manipulation of the arm and assisted by virtual environments, innovative interaction schemes are explored in search of the best possible therapy. Overall, robot assisted therapy is considered to be as good or better then conventional therapy [1], [2], [3], [4]. Robot assisted therapy is more challenging for the patients and less labor intensive for the therapists, and provides the physicians, therapists and scientific community with more objectively gathered data.

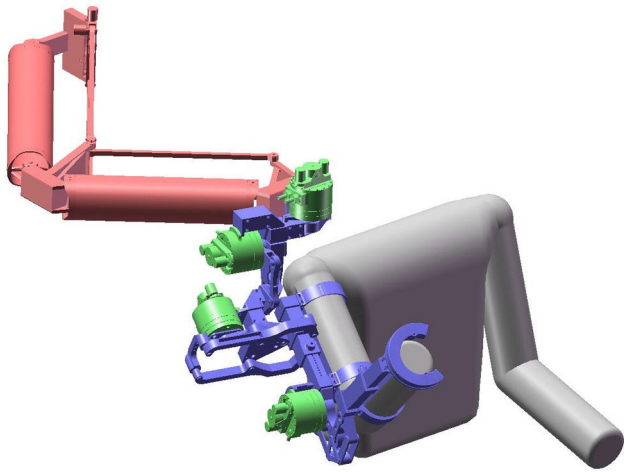

Fig. 1. The design of the upcoming torque-driven exoskeleton, the Limpact. It has self-aligning joints in the exoskeleton (blue), made possible by a freely translating but rotational stiff linkage (red). The four rHEAs (green) are positioned such that the flexible tubes (not displayed) do not interfere with each other.

Systematic reviews on non-robotic therapy for the upper-extremities also indicate that intensive and task-specific exercises consisting of active, repetitive movements, give the best results [5], [6], [7], [8]. Actively generated movements requires more brain activity and results in better motor learning, when compared to externally-powered arm movements without active patient participation [9]. But for all this, it is important to remember that improved motor control is not necessarily enough to restore lacking functional ability.

With our Freebal [10] and Dampace [11], we already created two devices for rehabilitation therapy. The Freebal supports the arm against gravity via a passive cable-pulley system, and facilitates shoulder and elbow movements without disturbing normal motor control [12], [13], [14]. The Dampace is a passive, self-aligning exoskeleton, which actively controls resistance torques on the shoulder and elbow joints.

As passive devices, both the Freebal and the Dampace force the patients to actively participate. In a three step process of identification, isolation, and integration—that is, identifying causes behind the movement disorder, tackling these with isolated, impairment-directed training, possibly over multiple joints, and then integrating the improvements

This work was supported by SenterNovem (NL) grant TSGE2050.

[1] Laboratory for Biomechanical Engineering, University of Twente, PO Box 217, 7500 AE Enschede, NL.

[2] BAAT Medical, Hengelo, NL.

[3] Biomechanical Engineering, Delft University of Technology, Delft, NL.

[4] Neuro Imaging and Motor Control Laboratory, Northwestern University, Chicago, Illinois, USA.

Corresponding author: Arno Stienen (arnostienen@gmail.com)

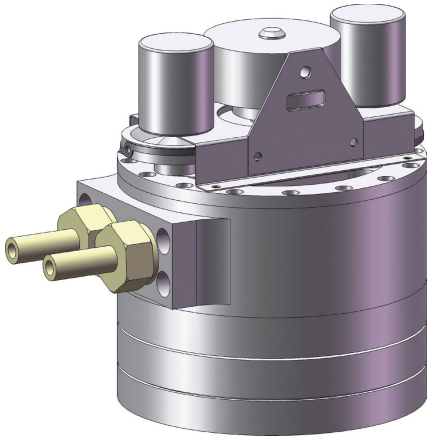

Fig. 2. Rotational hydro-elastic actuator (rHEA), a rotational variant of the linear HEA [18], in a compact design [19], [20], for use on our upcoming exoskeleton, the Limpact.

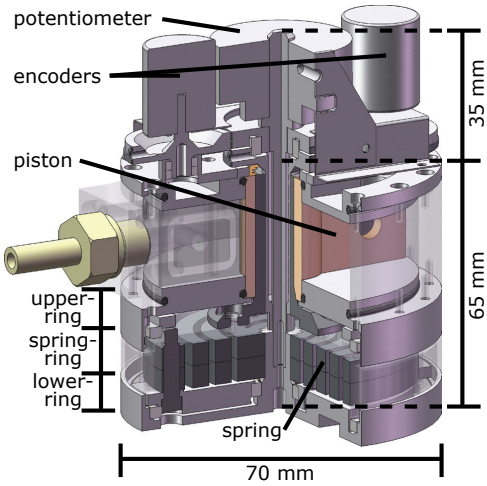

Fig. 3. Open view of the rHEA. From top to bottom: the angular sensors, the hydraulic actuator, and the spring.

via functional, task-specific training back into activities of daily living—they are well suited for the last two stages. But passive devices are not always appropriate for identification. For example, for separating intrinsic and reflexive components of human arm dynamics [15], active devices are needed to trigger the human system. With an active device, it is also possible to provide assist as needed [16] and create more realistic virtual environments [17].

In the LOPES project for the lower extremities [21], we have had good experiences with series elastic actuation (SEA) [22]. The SEA makes highly-compliant impedance control for the LOPES joints possible [23], despite high and highly variable friction forces in its Bowden cables. More in general, a SEA has low output impedance and good back-drivability, force output resolution and force control, as compared to directly connected electro motors with gearboxes. SEA does not require a perfect model of the entire actuator to operate, as the actuator is controlled on the direct measurement of the spring deflection. This spring deflection measures the applied forces at the point of application at the end of the force chain, allowing the SEA controller to reject most of the system noise, non-linearities and interfering dynamics which entered the chain at any previous point. These properties make SEA a good choice for a powered exoskeleton for the arm.

We concluded we need an active device, staying close to the Dampace mechanical design and using SEA as its power source. The goal of this paper is to describe the design of our SEA and validate its characteristics for suitability for powering our new exoskeleton, the Limpact (see Fig.1).

II. Requirements

The SEA should be able to deliver 50 Nm of torque with a bandwidth of 5 Hz. This is needed for weight support of exoskeleton and arm, measuring spasticity in stroke, and triggering the internal human systems for identification. For more conventional therapy exercises and simple virtual environments, 5 Nm at about 20 Hz is sufficient. The delivered torque resolution should be below 1 Nm, and the measured torque resolution below 0.1 Nm. The minimal impedance, the torque felt when moving the arm while no torque is requested, is preferably as low as possible. Isometric torques need to be measured at up to 100 Nm, but additional mechanisms may be used to make this possible. The final design should weigh less than 1.5 kg, to be directly mountable on an exoskeleton.

Most other requirements for our SEA result from the overall design of the Limpact exoskeleton. Like in the LOPES project [21], electric motors and gearboxes which can deliver the required power are too heavy to directly mount on the exoskeleton. LOPES uses Bowden cables to connect the motors on the base frame to the series elastic elements on the joints. The required cable pretension results in large amounts of non-linear friction which fluctuates strongly with cable orientation changes due to exoskeleton movements, up to 40% of maximum torque, and a lot of wear and tear. The SEA can compensate for most of the friction, but not all. An arm exoskeleton has much larger joint rotations than one for the legs, resulting in more cable bending and thus more unpredictable friction.

For the Limpact, we chose to replace the Bowden cables with hydraulic actuation, while keeping the series-elastic element. The rotational hydraulic actuators are mounted directly on the joints, but the large servo valves are not. These are placed on the base frame, connected to the actuators via 2 m long flexible tubes. Tube dynamics, and other effects like piston friction, are better predictable and much less variable with movement then the friction forces in Bowden cables, and any remaining unknown dynamic effects are account for by the aforementioned principle of SEA. The resulting rotational hydro-elastic actuator (rHEA) is a rotational variant of the linear HEA [18].

Fig. 4. Symmetric torsion spring of strong yet malleable maraging steel, were the reaction forces of both windings are canceled out, keeping spring center always in the middle.

III. Design

The rHEA design (see Fig.2) is a combination of a symmetric torsion spring, an hydraulic actuator, and high precision quadrature encoders. The overall design weighs less than 1.5 kg, including oil, but excluding the weight of the flexible tubes. At 70x100mm, it is very compact (see Fig.3). The springs is at 0.150 kg the heaviest component and is located at the bottom of the rHEA; the lightest elements, the sensors, are positioned on top, resulting in the best possible weight distribution.

The design has three rings at the bottom. The upper ring is connected to the base of the hydraulic actuator, the middle spring ring to the output of the hydraulic actuator and the base of the spring, and the lower ring to the output of the spring and total rHEA. At the elbow, for instance, the upper ring is fixed to the upper arm and the lower ring to the lower arm. The difference between the lower ring and the spring ring, times the spring stiffness, is the actuator torque. The spring deflection is limited to the maximum desired torque by a chamber in the lower ring. By locking the lower and spring ring together, the spring is bypassed and the rHEA can be used as a regular spring-less hydraulic actuator. Locking all three rings together sets up the actuator for isometric measurements up to 100 Nm, with the torque measured by strain gauges in the lower ring.

A. Symmetric torsion spring

The most important element in a SEA design is the elastic element. The spring stiffness should be chosen carefully; too low and it reduces the torque bandwidth, too high and it increases the impedance and worsens the torque output resolution [22]. With recommendations from literature [18] and based on our experience with LOPES, we selected a desirable stiffness of about 150 Nm/rad.

In another compact SEA design [19], [20], they used a spandrel-shape torsional spring with a stiffness of 327 Nm/rad. This long torsional spring runs through the center of their frameless motor and gearbox, but our hydraulic actuator has no room for such a solution. Besides this, for our desired torque output resolution, their spring stiffness is too high and their maximum permissible torque too low. Lowering the spring stiffness with equal or higher maximum strength and equal dimensions, is not trivial.

To fit in our compact design, the torsion spring has to be flat like a clock spring. Wrapping or unwrapping a clock spring offsets the middle of the spring, resulting in large loads on the bearings and deformations in the construction. Using two symmetric windings cancels their offsetting forces (see Fig. 4), at the cost of needing more material to achieve the same maximum strength and spring stiffness. By using maraging steel (type 18Ni, alloy 350), which has a high yield stress of 2400 MPa and is very tough, resilient and malleable, the dimensions of the spring need only be 10 mm high, 60 mm in diameter and with 4.5 mm thick windings for a maximum strength of 50 Nm and an expected spring stiffness of 150 Nm/rad. The springs are made by electrical discharge machining.

Our finite element program (COSMOSWorks, Dassault Systemes) could not handle the large deformations in our original spring design. This first spring, used in the validation experiments below, was 50 mm in diameter, with 3.5 mm thick windings, and was a lot less stiff (88 Nm/rad) than the intended 125 Nm/rad. The windings touched each other at 22 Nm, long before the intended maximum torque of 50 Nm. Overall, the oval shape deformation of the windings was much flatter in the real spring then predicted. Therefore, the spring for our final rHEA design for the Limpact has been scaled to the aforementioned dimensions.

As a rule of thumb, the thicker the winding or the overall spring, the higher the allowable torque and the stiffer the spring. Longer windings reduce the spring stiffness, but need more room to wrap and unwrap. Best results are achieved when the windings just touch when the maximum torque is reached, as this acts as an integrated safety mechanism to reduce overstretching of the outside of the windings.

B. Sensors

In the rHEA, two ultra miniature, high resolution quadrature kit encoders (Avago AEDA-3300 Series, $N_{ppr} = 80000$ pulses per revolution) measure the angle between the upper and lower ring, and between the upper and spring ring. The difference between the two encoders is equal to the deflection of the spring. By multiplying the deflection with the spring stiffness, the encoders function as torque sensor with a resolution equal to $2\pi K_{spr}/N_{ppr} \approx 0.01\ Nm$, with K_{spr} the spring stiffness.

The angle between the upper and lower ring is also measured by a potentiometer to initialize one of the encoders and signal any sensor malfunctions. Strain gauges at the lower ring have the same function for the other encoder, and will also measure the torque on the actuator during isometric measurements.

C. Control model

One of the advantages of using an elastic element at the final end of the actuation chain is the use of straightforward control schemes. No complex hydraulic modeling of the rHEA is required, as just the relative displacement of the

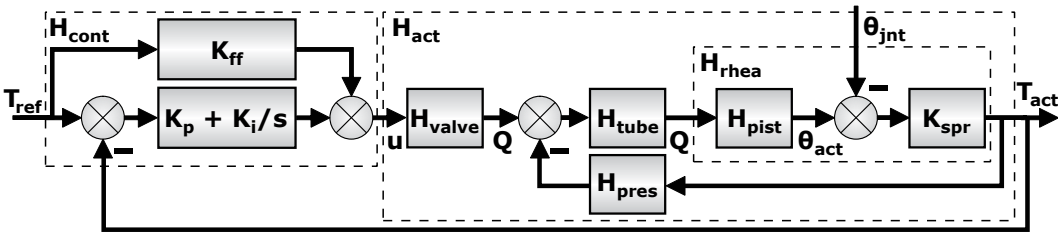

Fig. 5. rHEA control diagram, with the feedforward gain K_{ff}, and proportional and integrator gain settings K_p and K_i [18] as the controller H_{cont}. H_{valve} represents the hydraulic valve, H_{tube} the tube dynamics of the 2 m long flexible tubes, H_{pist} the rotational piston in the rHEA H_{rhea}, and K_{spr} the rotational spring stiffness, which together form the complete actuator H_{act}. The actuator torque T_{act} is measured by multiplying the deflection of the spring ($\theta_{act} - \theta jnt$) with K_{spr}.

spring is controlled. On the linear hydro-elastic actuator (HEA) [18], they used a standard PI controller. The control diagram for our rHEA is similar (see Fig. 5), but has an additional feedforward gain K_{ff} parallel to the PI controller $(K_p + K_i/s)$. The feedforward gain sets the opening of the hydraulic valve to get a known displacement of the spring. This prior knowledge results in less tracking error, enabling higher feedback gains of the PI controller, improving overall performance.

Although almost no modeling is needed to control the rHEA, and we tuned our PI-controller without it, to assist our analysis of the rHEA in open en closed-loop situations we fitted several models based on the generic control diagram in Fig. 5 on the measured results. The following analysis is based on the HEA of Robinson and Pratt (2000, denoted below by 'rp') [18]. To get from their linear, force controlled HEA to our rotation, torque controlled rHEA, we made some changes: each force F is replaced by torque T, displacement x by angle θ, and piston area A by piston area times the radius to the piston area center Ar, with A equal to 420 mm^2 and r to 16 mm, and we added the tube dynamics H_{tube} and possible pressure feedback H_{pres}.

The original components of the generic control diagram [18], converted to our rotation actuator, are:

$$\begin{aligned} H_{valve,rp}(s) &= \frac{K_{v,rp}}{(\tau_1 s+1)} \text{ or} \\ &= \frac{K_{v,rp}}{(\tau_1 s+1)(\tau_2 s+1)(\tau_3 s+1)}, \\ H_{tube,rp}(s) &= 1, \\ H_{pist,rp}(s) &= \frac{1}{Ars}, \\ H_{pres,rp}(s) &= 0, \end{aligned} \tag{1}$$

in which the H_{valve} is a first or third order approximation of the valve dynamics, converting a control signal opening the hydraulic valve u to a hydraulic flow Q, based on the valve gain $K_{v,rp}$ and the time delays τ_{1-3}. The rotational piston H_{pist} in the rHEA displaces the spring by an angle θ_{act} based on the delayed incoming flow Q. After subtracting the joint displacement angle θ_{jnt}, the spring displacement is multiplied with the rotational spring stiffness K_{spr}.

We changed the actuator model H_{act} to account for some of the valve-flow dependency on the pressure drop caused by the increase of pressure feedback due to the deflected spring [18]:

$$Q_{max} = K\sqrt{P_s - \frac{T_{act}}{Ar}}, \tag{2}$$

by reducing the valve flow Q with a rough linearized gain approximation K_{pf} in the pressure feedback H_{pres}. As these effects were originally captured in the valve model $H_{valve,rp}$, we simplified this model to a direct gain. We also added a transport delay H_{tube}, mimicking the effects of our long tubes by delaying flow Q trough the tubes by τ_2. The components of our control diagram now become:

$$\begin{aligned} H_{valve}(s) &= K_v, \\ H_{tube}(s) &= e^{-s\tau_2}, \\ H_{pist}(s) &= \frac{1}{Ars}, \\ H_{pres}(s) &= \frac{K_{pf}}{Ar}. \end{aligned} \tag{3}$$

The complete power chain H_{act} of valve, tube and rHEA and the frequency response function of the entire controlled system H_{sys}, are given by:

$$\begin{aligned} H_{act}(s) &= \frac{H_{valve}H_{tube}H_{pist}K_{spr}}{1+(H_{tube}H_{pist}K_{spr}H_{pres})}, \\ H_{sys}(s) &= \frac{(K_{ff}+K_p+\frac{K_i}{s})H_{act}}{1+(K_p+\frac{K_i}{s})H_{act}}. \end{aligned} \tag{4}$$

IV. Validation

The open-loop and closed-loop performance of the rHEA was measured by output torque tracking with fixed angular output θ_{jnt} to get the torque bandwidths, and maintaining zero output torque during angular disturbances to get the minimal impedance. Step responses and virtual springs show some general uses of the rHEA.

For these measurements, we used the test setup in Fig. 6. The generic hydraulic pump and external accumulator delivered a close to constant source pressure P_s of 8 MPa throughout the tests. The servo valve used was the Parker D1FP-E50M-9NS00, connected to flexible tubes rated for a maximum of 120 MPa and with a 6 mm inner diameter.

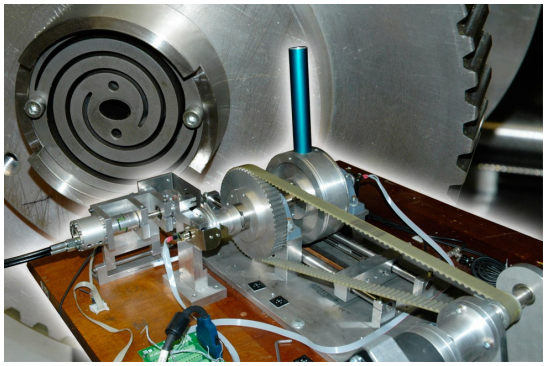

Fig. 6. Experimental setup, in which the hydraulic actuator (left mid), spring (mid and background) and sensors were mounted separately to ensure access during testing. The actuator drives the inside of the torsional spring, with the outside of the spring mounted to the large gear wheel. By fixing the gear wheel, the base of the springs stays static. The impedance is measured by powering the gear wheel with the large electro motor (bottom right). Finally, by freeing the gear wheel and using the top handlebar, we manually interacted with the controllers.

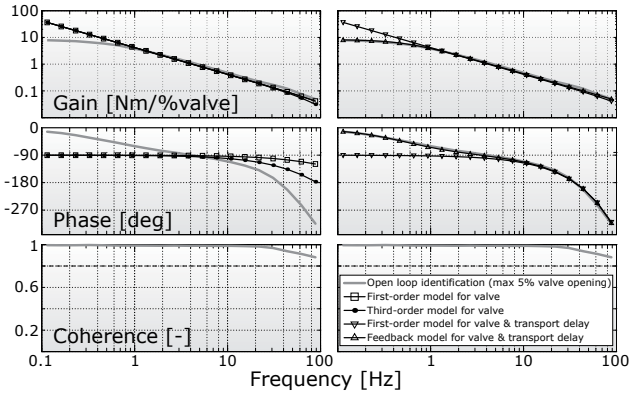

Fig. 7. Bode plot of the open-loop identification of the complete actuator $H_{act,ol} = T_{act}/u$. The open-loop results were fitted with actuator models $H_{act,ol1-4}$ consisting of the valve, tube, piston and spring components. $H_{act,ol1}$: line with open squares, $H_{act,ol2}$: line with closed circles, $H_{act,ol3}$: line with downwards pointing triangles, $H_{act,ol4}$: line with triangles pointing up. $H_{act,ol4}$ clearly results in the best fit.

A. Multi-sine identification

For the open- and closed-loop identification, we perturbed the system with multi-sine input signals to estimate the frequency response $C(s)$ and squared coherence $Coh(s)$ functions. These functions were estimated with cross- and auto-spectral densities $S(s)$ of input (i) and output (o) [24], [25], [15]. For a black-box system with single input and single output, the functions are:

$$C(s) = \frac{S_{io}(s)}{S_{ii}(s)},$$
$$Coh(s)^2 = \frac{|S_{io}(s)|^2}{S_{ii}(s)S_{oo}(s)}. \quad (5)$$

The frequency response function $C(s)$ is an estimate for the dynamics of the black-box system, and the squared coherence function $Coh(S)$ a measure for the signal to noise ratio at each frequency. The squared coherence [26] ranges from zero to one, with zero meaning the lack of correlation between the input and output, and one the absence of noise or time-varying behavior. Higher harmonics in periodic signals may interfere with the interpretation of the coherence function.

For all but the minimal-impedance measurements, the input perturbation signal consisted of 80 summed sines of 256 seconds. The frequencies of the sines were spaced logarithmical from 0.1 to 100 Hz, were of constant power spectral density, and had random phase shifts to reduce amplitude peaks in the summed signal. Due to the lack of motor power for external disturbance in the minimal-impedance measurements, this multi-sine input signal was limited to 64 sines, spaced from 0.1 to 25 Hz.

The logarithmical spacing of the sine frequencies prevented the use of crest optimization on the total signal. Therefore, the amplitude of the total signal was scaled on two or three times the standard deviation and not the peak-to-peak values, with the mean of the signal always at zero. Measurements were repeated four times with four uniquely generated multi-sine signals, differing on the used random phases. The results were averaged in the frequency domain over four frequencies and the four repetitions to improve the coherence of the measurements and estimates.

B. Open-loop actuator

For the open-loop identification of the actuator $H_{act,ol} = T_{act}/u$, the controller H_{cont} was disabled, the output position $theta_{jnt}$ fixed, and the valve opening signal u fed with a 0.1-100 Hz multi-sine, with three times the standard deviation equal to 5% valve opening. At 5% the spring would already be rotated to generate its maximum torque output of 22 Nm and restricted from rotating further. More valve opening contributing to increasing the rotational piston speed when the spring was not already at the maximum torque output.

The identified frequency response function of the complete actuator $H_{act,ol}$ was fitted with the following models:

$$H_{act,ol1}(s) = \frac{K_{v,rp}}{(\tau_1 s+1)s}\frac{K_{spr}}{Ar}, \quad (6)$$
$$H_{act,ol2}(s) = \frac{K_{v,rp}}{(\tau_1 s+1)(\tau_2 s+1)(\tau_3 s+1)s}\frac{K_{spr}}{Ar}, \quad (7)$$
$$H_{act,ol3}(s) = \frac{K_{v,rp}}{(\tau_1 s+1)s}\frac{K_{spr}}{Ar}e^{-s\tau_2}, \quad (8)$$
$$H_{act,ol4}(s) = \frac{K_v/K_{pf}}{(Ar/(K_{spr}K_{pf}e^{-s\tau_2}))s+1}. \quad (9)$$

$H_{act,ol1}$ is the direct adaptation of the HEA actuator model [18], with a first-order valve model and without any additional tube dynamics. $H_{act,ol2}$ is the same, except it uses a third-order valve, also from the HEA [18]. $H_{act,ol3}$ follows directly from Eq. 4 and 4, and now include a transport delay as model for the tube dynamics H_{tube}. $H_{act,ol4}$ is our adapted actuator model which uses the pressure feedback. In effect, it is the same as $H_{act,ol3}$ but with the pure integrator from the piston model H_{pist} converted into a first-order system due to the pressure feedback.

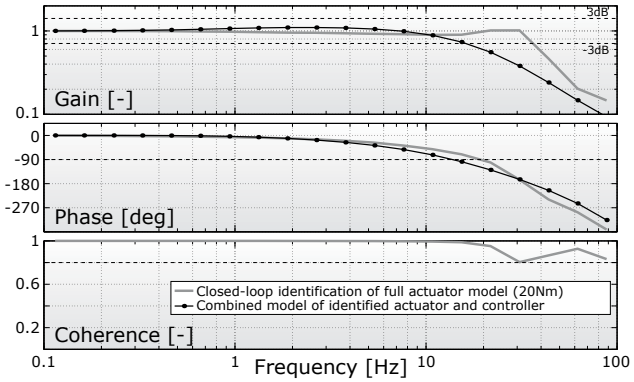

Fig. 8. Bode plot of the closed-loop frequency response function $H_{sys,cl} = T_{act}/T_{ref}$ for the 20 Nm multi-sine reference torque (the gray line). The best fitting actuator model ($H_{act,ol4}$) was combined with the system model H_{sys}. With the closed-loop control gains, the fit was far from perfect (line with filled circles).

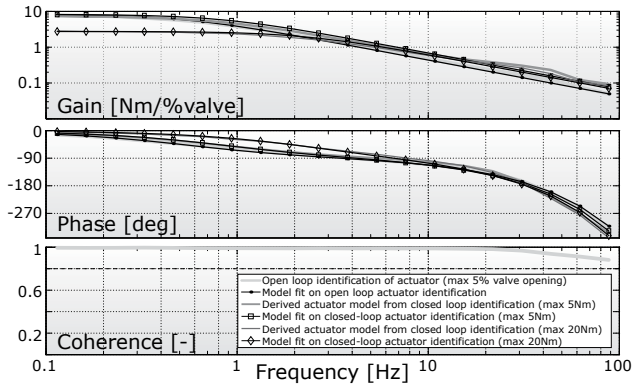

Fig. 9. Bode plot of the open-loop identified $H_{act,ol}$ and closed-loop estimated actuators $H_{act,cl05}$ and $H_{act,cl20}$. The behavior of the identified actuator (light-gray line) and the closed-loop estimated for the 5 Nm amplitude (gray line with closed circles) closely resembles each other. For the 20 Nm amplitude, the closed-loop actuator (dark-gray line with open squares) is significantly shifted in the gain and phase lag plots. For all identified actuators, the best fitting actuator model $H_{act,ol4}$ fitted the data close to perfect.

The identified open-loop actuator and the four model fits are given in Fig. 7. The first two models ($H_{act,ol1-2}$) fit the data badly. Not only does the low-frequency gain not match, the pure integrator in the model keeps the low-frequency phase lag at 90°, while the identified actuator approaches 0°. They also do not match the high-frequency phase, at least not without significant distortion to the high-frequency gain. Adding a transport delay as the model for the tube dynamics H_{tube} does improve the fit on the high-frequency phase for $H_{act,ol3}$, but still doesn't give a match the low-frequency gain and phase. As the pressure feedback model $H_{act,ol4}$ has lost the pure integrator, it fits perfectly on the identified open-loop actuator. The parameters for the fits of Fig. 7 are found in Tab. I, were K_{system} is the system gain of each model, and τ_1 the time-constant equivalent for the first order system of $H_{act,ol4}$.

C. Torque bandwidth

The frequency response function of the close-loop system $H_{sys,cl} = T_{act}/T_{ref}$ was identified by letting it track a 0.1-100 Hz multi-sine reference torque T_{ref}, with three-times the standard deviation equal to 20 Nm (see Fig. 8), with the output position $theta_{jnt}$ fixed. The identified frequency response function has a -3 dB gain bandwidth of 35 Hz, and a 90° phase lag bandwidth of 18 Hz. The effects of the 2 m long tubes between the hydraulic valve and the hydraulic actuator are clearly seen by the rapidly increasing phase lag.

The best fitting actuator model ($H_{act,ol4}$) was combined with the system model H_{sys}. With the closed-loop control gains ($K_{ff} = 0.15$, $K_p = 1.85$, $K_i = 10$), the fit of the complete system $H_{sys,cl}$ was far from perfect, indicating the presence of non-linearities as saturation in the actuator. The reduced coherence at the resonant peak is due to the spectral averaging over four frequencies, which is no reason for concern.

With the used control gains known, the actuator can be reverse estimated from the closed-loop identification $H_{sys,cl}$ by rewriting (Eq. 4):

$$H_{act,cl}(s) = \frac{H_{sys,cl}}{(K_{ff} + K_p + \frac{K_i}{s}) - (K_p + \frac{K_i}{s})H_{sys,cl}}. \quad (10)$$

The frequency response function of these actuator estimations $H_{act,cl05}$ and $H_{act,cl20}$, estimated from the closed-loop frequency response functions at respectively 5 Nm and 20 Nm (three times standard deviation) desired torque amplitudes, are compared to the actuator $H_{act,ol}$ from the the open-loop identification in Fig. 9. The previously best-fitting model ($H_{act,ol4}$) was fitted to each estimation (see Tab. II). The behavior of the identified open-loop actuator and the closed-loop actuator at 5 Nm closely resembles each other, but at 20 Nm amplitude, the closed-loop actuator is significantly shifted in the gain and phase lag plots, indicating the saturation and other non-linearities of the valve-flow modeling in the actuator. Again, the simplest first-order actuator model $H_{act,ol4}$ closely fitted all actuator frequency response functions, except for the measured gain

TABLE I
PARAMETERS TO FIT MODELS $H_{act,ol1-4}$ TO IDENTIFIED $H_{act,ol}$ (FIG. 7).

		K_{system}	τ_1	τ_2	τ_3
$H_{act,ol1}$	Eq. 6	26	¿0.001	-	-
$H_{act,ol2}$	Eq. 7	26	¿0.001	¿0.001	¿0.001
$H_{act,ol3}$	Eq. 8	26	¿0.001	0.006	-
$H_{act,ol4}$	Eq. 9	8.3	0.300	0.007	-

TABLE II
PARAMETERS TO FIT MODEL $H_{act,ol4}$ TO IDENTIFIED $H_{act,ol}$, $H_{act,cl05}$ AND $H_{act,cl20}$ (FIG. 9).

	K_{system}	τ_1	τ_2
$H_{act,ol}$	8.3	0.30	0.0070
$H_{act,cl05}$	8.3	0.19	0.0075
$H_{act,cl20}$	2.6	0.07	0.0080

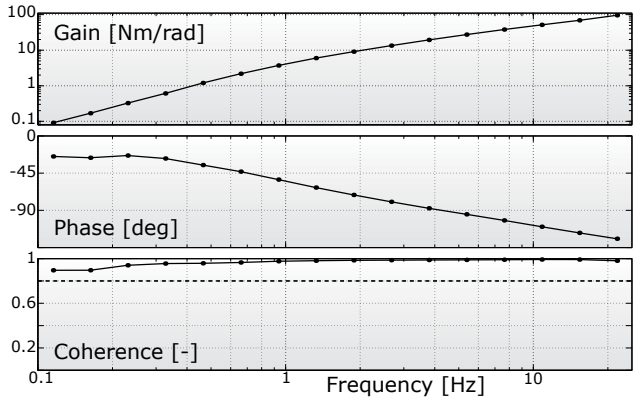

Fig. 10. Bode plot of the minimal impedance measurements, with impedance $H_{img} = T_{act}/\theta_{jnt}$. For these measurements, the references torque T_{ref} is 0 Nm, while the angular position θ_{jnt} was perturbed by a 0.1-25 Hz multi-sine with two times the standard deviation equal to 0.1 rad.

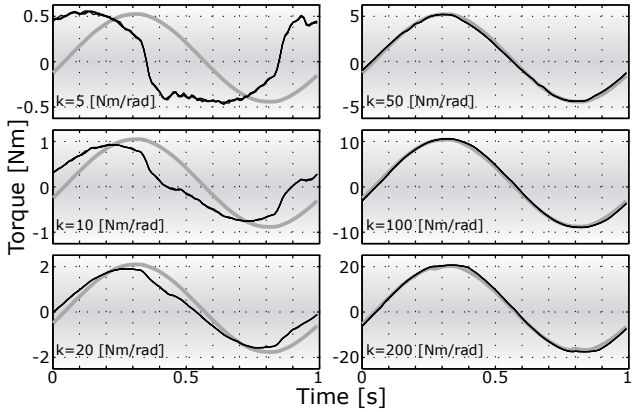

Fig. 12. Time plots of virtual springs. The external motor maintained a 1 Hz sine with a 0.1 rad amplitude on the angular position θ_{jnt}, while the virtual spring stiffness was increased from 5 to 200 Nm/rad. (Note the real spring stiffness of 88 Nm/rad.) The gray lines are the measured joint angles θ_{jnt} multiplied by the virtual spring stiffness, resulting in the desired torque signal T_{ref}. The recorded actuator torques and plotted in black.

and phase-lag bumps at 30 Hz.

D. Minimal impedance

For the minimal impedance measurements (see Fig. 10), the references torque T_{ref} is 0 Nm, while the angular position θ_{jnt} provided by an external electro motor became the input to the system. The angular position θ_{jnt} was perturbed with a 0.1-25 Hz multi-sine with two times the standard deviation equal to 0.1 rad. Above 5 Hz, the external electric motor was not capable of maintaining the constant power spectral density and decayed slightly, but this should not be a problem in Eq 5. The expected leveling of the gain at the spring stiffness (88 Nm/rad for the measured spring) at high frequencies was not achieved, as the external motor could not reach these. Extrapolating, it should start at about 25 Hz, above which only the physical spring characteristics of SEA are felt.

E. Step response

In the step responses of Fig. 11, four different torque steps responses are plotted for eight repetitions per step size. Overshoot and response time are all acceptable for our purposes, although using an better inverse model for the feedforward control H_{ff}, as opposed to the current linear gain K_{ff} in Fig. 5, may further improve the results. The variability of the response overshoot and settling-time indicates non-linearities are present in the physical rHEA.

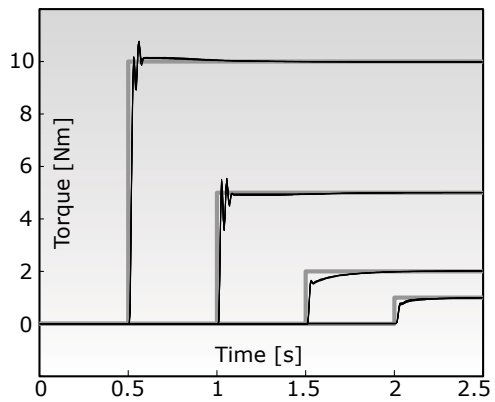

Fig. 11. Time plots of step reference signals. In gray, the required torque T_{ref}. In black, the measured torques T_{act}.

F. Virtual spring

To illustrating the power of impedance control, virtual springs of different stiffness were created. The rHEA had to respond to a angular displacement θ_{nnt} as if it was a spring with a stiffness ranging from 5 to 200 Nm/rad. The angular displacement was realized by the external electro motor, and consisted of a 1 Hz sine with a 0.1 rad amplitude. Based on these results and experimental experience, the minimal stiffness was limited by the minimal output torque required and not necessarily the lowness of the virtual stiffness. Below 1 Nm, even though the controller could realize the required output torque resolution, it also generates phase-lead, probably because of unaccounted valve and tube dynamics and piston friction. The 200 Nm/rad upper limit of the virtual spring stiffness was the result of the maximum actuator torque T_{act} of 22 Nm and the 0.1 rad reference amplitude. Increasing the first or lowering the second makes higher virtual spring stiffness possible, although a system with high virtual stiffness might need an input filter to ensure stable operations at every frequency [27].

V. Discussion and conclusions

After the validation measurements, the results are mixed. The torsion spring did not reach the desired maximum torque of 50 Nm and was weaker than expected. The multi-sine torque bandwidth of at least 18 Nm, measured torque resolution of 0.01 Nm, and the torque output resolution of less then 1 Nm are more than acceptable. The weight of the rHEA is at 1.3 kg below the maximum of 1.5 kg. When the minimal impedance and modeled virtual springs were felt by manually rotating the actuator output via a stick,

almost no torque distortion was felt, even when manipulating with forefinger and thumb. By manually locking of the outer rings, the rHEA can also operate as a stiff hydraulic actuator, when disabling the spring ring, or as an isometric measurement device, when locking all three rings together. A stiff hydraulic actuator in admittance control can achieve more precise and faster position perturbations, as compared to impedance control of SEA. Using an interactive approach to achieve the optimal spring characteristics, the latest rHEA has the desired 50 Nm of maximum output torque and is to be mounted on our new exoskeleton, the Limpact (see Fig.1).

The modified theoretical model of the actuator, based on the work of Robinson and Pratt [18], had a good fit to the measured open-loop frequency response of the actuator. To recreate the time lags as observed in the response function, we added a transport delay to the original actuator model, which improved the high-frequency fit. But only when we added a rough approximation of pressure feedback to the actuator model, in effect removing the pure integrator, did we reach an almost perfect fit to the gain and phase lag at high and low frequencies. Comparison to the original study [18] is difficult, as the fit they showed of the open-loop actuator did not include frequency responses below 2 Hz. Based on what can be seen, we believe our adapted model might better fit their actuator measurements too, as (1), their low-frequency phase response seems to start with less then 90° phase lag, and (2), their phase lag at high-frequency keeps on dropping, where their third-order valve model and pure integrator should level out at 360°. We also speculate that more realistic and non-linear valve-flow functions based on both pressure drop over the valve and the valve opening (see Eq. 2), may result in better future models.

REFERENCES

[1] J. Van der Lee, I. Snels, H. Beckerman, G. Lankhorst, R. Wagenaar, and L. Bouter, "Exercise therapy for arm function in stroke patients: a systematic review of randomized controlled trials." *Clin Rehabil*, vol. 15, no. 1, pp. 20–31, Jan 2001.

[2] T. Platz, "Evidence-based arm rehabilitation - a systematic review of the literature." *Nervenartz*, vol. 74, no. 10, pp. 841–849, Oct 2003.

[3] G. Prange, M. Jannink, C. Groothuis-Oudshoorn, H. Hermens, and M. IJzerman, "Systematic review of the effect of robot-aided therapy on recovery of the hemiparetic arm after stroke." *J Rehabil Res Dev*, vol. 43, no. 2, pp. 171–184, 2006.

[4] G. Kwakkel, B. J. Kollen, and H. I. Krebs, "Effects of robot-assisted therapy on upper limb recovery after stroke: A systematic review." *Neurorehabil Neural Repair*, Sep 2007.

[5] R. Schmidt and T. Lee, *Motor control and learning.*, 3rd ed. Champaign, IL, USA: Human Kinetics Publishers, 1999.

[6] G. Kwakkel, R. Wagenaar, J. Twisk, G. Lankhorst, and J. Koetsier, "Intensity of leg and arm training after primary middle-cerebral-artery stroke: a randomised trial." *Lancet*, vol. 354, no. 9174, pp. 191–196, Jul 1999.

[7] S. Barreca, S. Wolf, S. Fasoli, and R. Bohannon, "Treatment interventions for the paretic upper limb of stroke survivors: a critical review." *Neurorehabil Neural Repair*, vol. 17, no. 4, pp. 220–226, Dec 2003.

[8] H. Feys, W. De Weerdt, G. Verbeke, G. Steck, C. Capiau, C. Kiekens, E. Dejaeger, G. Van Hoydonck, G. Vermeersch, and P. Cras, "Early and repetitive stimulation of the arm can substantially improve the long-term outcome after stroke: a 5-year follow-up study of a randomized trial." *Stroke*, vol. 35, no. 4, pp. 924–929, Apr 2004.

[9] J. Liu, S. Cramer, and D. Reinkensmeyer, "Learning to perform a new movement with robotic assistance: comparison of haptic guidance and visual demonstration." *J Neuroengineering Rehabil*, vol. 3, p. 20, 2006.

[10] A. Stienen, E. Hekman, F. Van der Helm, G. Prange, M. Jannink, A. Aalsma, and H. Van der Kooij, "Freebal: dedicated gravity compensation for the upper extremities." in *Proc 10th ICORR'07*, B. Driessen, J. Herder, and G. Gelderblom, Eds. Noordwijk, the Netherlands: IEEE Operations Center, Piscataway, USA, Jun 13-15 2007.

[11] A. Stienen, E. Hekman, F. Van der Helm, G. Prange, M. Jannink, A. Aalsma, and H. Van der Kooij, "Dampace: dynamic force-coordination trainer for the upper extremities." in *Proc 10th ICORR'07*, B. Driessen, J. Herder, and G. Gelderblom, Eds. Noordwijk, the Netherlands: IEEE Operations Center, Piscataway, USA, Jun 13-15 2007.

[12] M. Jannink, G. Prange, A. Stienen, H. Van der Kooij, J. Kruitbosch, M. IJzerman, and H. Hermens, "Reduction of muscle activity during repeated reach and retrieval with gravity compensation in stroke patients," in *Proc 10th ICORR'07*, B. Driessen, J. Herder, and G. Gelderblom, Eds. Noordwijk, the Netherlands: IEEE Operations Center, Piscataway, USA, Jun 13-15 2007.

[13] G. B. Prange, L. A. C. Kallenberg, M. J. A. Jannink, A. H. A. Stienen, H. van der Kooij, M. J. IJzerman, and H. J. Hermens, "Influence of gravity compensation on muscle activity during reach and retrieval in healthy elderly." *J Electromyogr Kinesiol*, Sep 2007.

[14] G. Prange, A. Stienen, M. Jannink, H. Van der Kooij, M. IJzerman, and H. Hermens, "Increased range of motion and decreased muscle activity during maximal reach with gravity compensation in stroke patients," in *Proc 10th ICORR'07*, B. Driessen, J. Herder, and G. Gelderblom, Eds. Noordwijk, the Netherlands: IEEE Operations Center, Piscataway, USA, Jun 13-15 2007.

[15] F. Van der Helm, A. Schouten, E. de Vlugt, and G. Brouwn, "Identification of intrinsic and reflexive components of human arm dynamics during postural control." *J Neurosci Methods*, vol. 119, no. 1, pp. 1–14, Sep 2002.

[16] E. T. Wolbrecht, V. Chan, D. J. Reinkensmeyer, and J. E. Bobrow, "Optimizing compliant, model-based robotic assistance to promote neurorehabilitation." *IEEE Trans Neural Syst Rehabil Eng*, vol. 16, no. 3, pp. 286–297, Jun 2008.

[17] T. Nef, M. Mihelj, and R. Riener, "Armin: a robot for patient-cooperative arm therapy." *Med Biol Eng Comput*, vol. 45, no. 9, pp. 887–900, Sep 2007.

[18] D. Robinson and G. Pratt, "Force controllable hydro-elastic actuator," in *Proc. IEEE International Conference on Robotics and Automation ICRA '00*, G. Pratt, Ed., vol. 2, 2000, pp. 1321–1327 vol.2.

[19] J. W. Sensinger and R. F. Weir, "Unconstrained impedance control using a compact series elastic actuator," in *Proc. 2nd IEEE/ASME International Conference on Mechatronic and Embedded Systems and Applications*, R. F. Weir, Ed., 2006, pp. 1–6.

[20] J. Sensinger and R. Weir, "User-modulated impedance control of a prosthetic elbow in unconstrained, perturbed motion," *IEEE Trans. Biomed. Eng.*, vol. 55, no. 3, pp. 1043–1055, 2008.

[21] J. Veneman, R. Kruidhof, E. Hekman, R. Ekkelenkamp, E. Van Asseldonk, and H. van der Kooij, "Design and evaluation of the lopes exoskeleton robot for interactive gait rehabilitation," *IEEE Trans. Neural Syst. Rehabil. Eng.*, vol. 15, no. 3, pp. 379–386, 2007.

[22] M. W. G.A. Pratt, "Series elastic actuators," in *Proceedings of the International Conference on Intelligent Robots and Systems*, vol. 1, Aug 1995, pp. 399–406.

[23] R. Ekkelenkamp, R. Ekkelenkamp, P. Veltink, S. Stramigioli, and H. van der Kooij, "Evaluation of a virtual model control for the selective support of gait functions using an exoskeleton," in *Proc. IEEE 10th International Conference on Rehabilitation Robotics ICORR 2007*, P. Veltink, Ed., 2007, pp. 693–699.

[24] G. Jenkins and D. Watts, *Spectral Analysis and Its Applications*. San Francisco, U.S.A.: Holden-Day, 1969.

[25] J. Bendat and A. Piersol, *Random Data: Analysis and Measurement Procedures*. New York, USA: Wiley, 1986.

[26] R. Pintelon and J. Schoukens, *System identification: a frequency domain approach*. New York, USA: IEEE Press, 2001.

[27] H. Vallery, J. Veneman, E. van Asseldonk, R. Ekkelenkamp, and H. Martin Buss Van der Kooij, "Compliant actuation of rehabilitation robots: Benefits and limitations of series elastic actuators," *IEEE Rob. Autom Mag.*, 2008 (In Press).